

# Sonochemical Preparation of Luminescent PbWO<sub>4</sub> Nanocrystals with Morphology Evolution

Jun Geng,<sup>†,‡</sup> Jun-Jie Zhu,<sup>\*,†</sup> and Hong-Yuan Chen<sup>†</sup>

*Department of Chemistry, Key Laboratory of Analytical Chemistry for Life Science, Nanjing University, Nanjing 210093, People's Republic of China, and Department of Chemistry, Jiangsu Institute of Education, Nanjing 210013, People's Republic of China*

*Received May 27, 2005; Revised Manuscript Received July 28, 2005*

**ABSTRACT:** PbWO<sub>4</sub> nanostructures with different morphologies, such as polyhedral, spindle-like, and dot-shaped, have been successfully synthesized via a mild sonochemical route from an aqueous solution of lead acetate and sodium tungstate in the presence of complexing reagent NTA. Reaction conditions, such as pH value and the concentration of complexing reagent, were found to have close relation with the morphologies of final products. The ultrasound-induced oriented attachment growth mechanism has been proposed for the possible formation mechanism of spindle-like sample. Raman and room-temperature photoluminescence of PbWO<sub>4</sub> samples with different morphologies have also been investigated.

## Introduction

Because the sizes and shapes of inorganic nanocrystals are important elements that determine their electrical, optical, and some other properties,<sup>1</sup> much effort has been explored for rational controlling over shape, size, dimensionality, and complexity of nanocrystals.<sup>2</sup>

In recent years, ultrasound has become an important tool in chemistry for its applications in the synthesis and modification of both organic and inorganic materials.<sup>3–5</sup> When liquids are irradiated with high-intensity ultrasound, acoustic cavitations (the formation, growth, and implosive collapse of the bubbles) provide the primary mechanism for sonochemical effects, during which very high temperatures (>5000 K), pressures (>20 MPa), and cooling rates (>10<sup>10</sup> K/s) can be achieved upon the collapse of the bubbles.<sup>6</sup> Such remarkable environments provide a unique platform for the growth of novel nanostructures.

Lead tungstate (PbWO<sub>4</sub>) has been attracting increasing attention because of its technological importance as an inorganic scintillating crystal. As compared to other well-known scintillators, PbWO<sub>4</sub> is most attractive for high-energy physics applications because of its high density (8.3 g/cm<sup>3</sup>), short decay time (less than 10 ns for a large part of light output), high-irradiation damage resistance (10<sup>7</sup> rad for undoped and 10<sup>8</sup> rad for La-doped PbWO<sub>4</sub>), interesting excitonic luminescence, thermoluminescence, and stimulated Raman scattering behavior.<sup>7,8</sup> PbWO<sub>4</sub> single crystals have usually been grown from the melt using the Czochralski<sup>9</sup> and Bridgman<sup>10</sup> methods. Several references reported the synthesis of PbWO<sub>4</sub> nano- and microcrystals with various morphologies by wet chemical methods.<sup>11–14</sup> However, it is still very important to develop some other convenient methods for the preparation of PbWO<sub>4</sub> in mild reaction conditions.

Herein, we introduce a facile and fast sonochemical route for preparing PbWO<sub>4</sub> crystals with controlled

morphologies and special optical properties. Studies found that some related experimental parameters including the pH value and the concentration of the complexing reagent have great influences on the morphologies of products. By carefully controlling these experimental parameters, PbWO<sub>4</sub> nanostructures of polyhedrons, spindles, and nanoparticles can be efficiently achieved, respectively.

## Experimental Section

All of the reagents used were of analytical purity and used without further purification. Pb(CH<sub>3</sub>COO)<sub>2</sub>·3H<sub>2</sub>O, Na<sub>2</sub>WO<sub>4</sub>·2H<sub>2</sub>O, and nitrilotriacetate acid (H<sub>3</sub>NTA) were purchased from Shanghai Second Chemical Reagent Factory (China). Absolute ethanol and KOH were purchased from Nanjing Chemical Reagent Factory (China). In a typical procedure, an aqueous solution of Pb(CH<sub>3</sub>COO)<sub>2</sub> in the presence of H<sub>3</sub>NTA was mixed with Na<sub>2</sub>WO<sub>4</sub> solution in a 150 mL round-bottom flask to give a final concentration of 20 mM Pb(CH<sub>3</sub>COO)<sub>2</sub>, 40 mM H<sub>3</sub>NTA, and 20 mM Na<sub>2</sub>WO<sub>4</sub>. The pH was adjusted to a specific value by KOH, and the total volume of the solution was 100 mL. The transparent mixture solution was then exposed to high-intensity ultrasound irradiation under ambient air for 2 h. Ultrasound irradiation was accomplished with a high-intensity ultrasonic probe (Xinzhi. Co., China, JY92-2D, 0.6 cm diameter; Ti-horn, 20 kHz, 60 W/cm<sup>2</sup>) immersed directly in the reaction solution. A white precipitate was centrifuged, washed with distilled water and absolute ethanol in sequence, and finally dried in air. The final products were collected for characterizations. The products were characterized via X-ray powder diffraction (XRD), transmission electron microscopy (TEM), selected area electron diffraction (ED), scanning electron micrographs (SEM), high-resolution transmission electron micrographs (HRTEM), Raman spectra, and photoluminescence spectra (PL).

The XRD analysis was performed on a Philips X'pert X-ray diffractometer at a scanning rate of 4°/min in the 2θ range from 10° to 80°, with graphite monochromatized Cu Kα radiation (λ = 0.15418 nm). SEM images were taken on a LEO-1530VP field-emission scanning electron microscope. TEM and ED patterns were recorded on a JEOLJEM 200CX transmission electron microscope, using an accelerating voltage of 200 kV. HRTEM were obtained by employing a JEOL-2010 high-resolution transmission electron microscope with a 200 kV accelerating voltage. Raman spectra were recorded on a JY HR-800 spectrometer provided by J. Y. Co. at room tempera-

\* Corresponding author. Telephone and fax: +86-25-83594976. E-mail: jjzhu@mail.nju.edu.cn.

<sup>†</sup> Nanjing University.

<sup>‡</sup> Jiangsu Institute of Education.

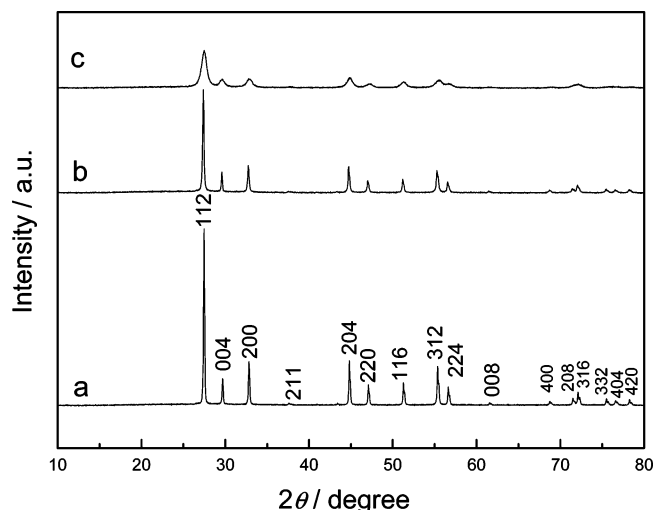


**Figure 1.** XRD patterns of products prepared at pH values of (a) 9.0, (b) 7.0, and (c) 5.0. The initial concentrations of  $\text{Pb}^{2+}$ ,  $\text{WO}_4^{2-}$ , and  $\text{H}_3\text{NTA}$  were 20, 20, and 40 mM, respectively.

ture and with an excitation wavelength of 488 nm. PL spectra were measured on a SLM48000DSCF/AB2 fluorescence spectrometer made by American SLM Inc. at room temperature.

## Results and Discussion

**Characterizations of Final Products.** Figure 1 shows the XRD patterns of the as-prepared products at different pH values with the same initial concentrations (20 mM  $\text{Pb}^{2+}$ , 20 mM  $\text{WO}_4^{2-}$ , and 40 mM  $\text{H}_3\text{NTA}$ ). The diffraction peaks of the products can be all indexed to a pure tetragonal stolzite structure with cell parameters  $a = 5.46$  and  $c = 12.04$  Å, which are in good agreement with the literature values (JCPDS Card Number 08-0476). However, on comparing the curves of the three products, we found that the relative intensity of the peaks varied significantly, which indicates different crystallinity. The samples prepared at pH 9.0 and 7.0 show better crystallization than the one made at pH 5.0. The broadening of the peaks in Figure 1c indicates that the crystallite size is small. The average particle size of the product is calculated to be ca. 11 nm according to the Debye–Scherrer equation.<sup>15</sup> These XRD patterns indicate that well-crystallized  $\text{PbWO}_4$  crystals can be easily obtained under the current synthetic conditions. The yields of  $\text{PbWO}_4$  crystals produced by this method are reproducibly about 70%.

The morphologies of final samples were observed with SEM and TEM techniques. Figure 2a shows that the

products prepared at pH 9.0 are polyhedrons with dimension of (400–500) nm × (600–700) nm. According to the projective image of TEM (Figure 2a) and the SEM images taken from different angles (Figure 3a–c), it is clear that the products are 18-faceted polyhedrons and the 4-fold symmetry of the structure can be identified (Figure 3d). The morphology of the products varied greatly when the pH value was decreased to 7.0 and the other conditions were kept the same. All of the samples are homogeneous spindle-like nanorods with diameters of 50–60 nm at the center and lengths of about 200–250 nm (Figures 2b and 3e). High-magnification SEM images (Figure 3b and f) reveal that the surfaces of the polyhedrons and spindles are not very smooth, indicating the existence of defects. Figure 2c shows the dot-shaped product prepared with a pH value of 5.0. The average size of these polycrystalline particles is about 10 nm, which agreed with the result calculated from the XRD pattern.

The HRTEM image recorded on the tip of a spindle (Figure 4a) shows that the sample is structurally uniform with an interplanar spacing of about 0.32 nm, which corresponds to the lattice spacing for the (112) faces of tetragonal  $\text{PbWO}_4$ . The HRTEM image of nanoparticles obtained under the pH 5.0 reaction system (Figure 4b) also indicates a clear crystal lattice with lattice spacing of 0.30 nm for (004) faces.

**Sonochemical Reaction Process.** The complexing reagent is a key factor in our experiments. Nitrilotriacetic acid ( $\text{H}_3\text{NTA}$ ) is one of the important derivatives of glycine and used in biochemistry and medicine.<sup>16–19</sup>  $\text{H}_3\text{NTA}$  is also a precursor of a multidentate organic ligand ( $\text{NTA}^{3-}$ ), incorporating carboxylic acid groups and one N-donor atom, capable of coordinating to several metal centers and also of eliminating available coordination sites.

The mechanism of the formation of  $\text{PbWO}_4$  nanocrystals is probably related to the coordination of  $\text{Pb}^{2+}$  and  $\text{NTA}^{3-}$  to form  $\text{Pb-NTA}$  complex, the dissociation of the complex under sonication, and formation of  $\text{PbWO}_4$ . The probable reaction process in aqueous solution can be summarized as follows:



An ultrasound wave that is intense enough to produce cavitations can drive chemical reactions such as oxidation, reduction, dissolution, and decomposition.<sup>20,21</sup> So



**Figure 2.** TEM images of samples prepared at pH values of (a) 9.0, (b) 7.0, and (c) 5.0. The initial concentrations of  $\text{Pb}^{2+}$ ,  $\text{WO}_4^{2-}$ , and  $\text{H}_3\text{NTA}$  were 20, 20, and 40 mM, respectively.

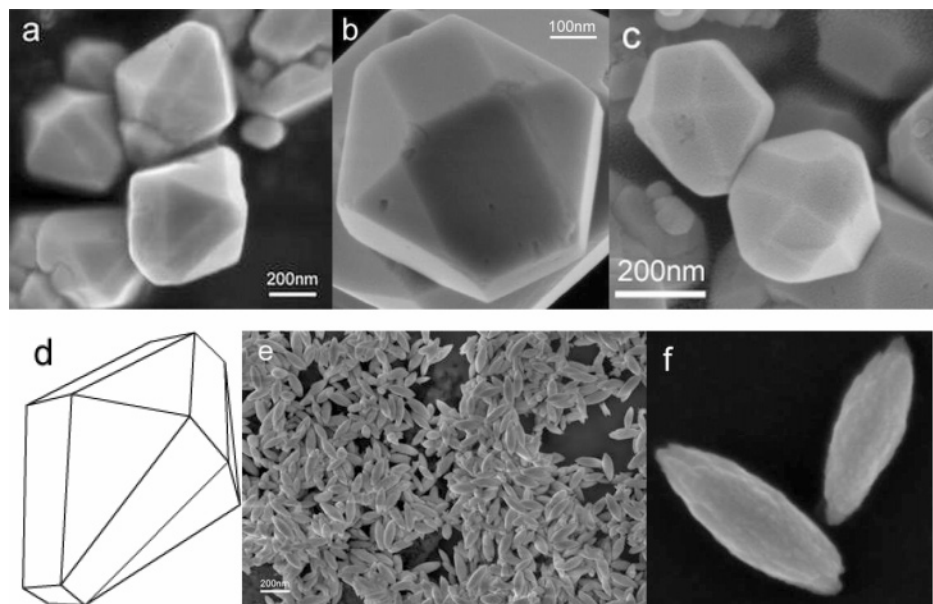


**Figure 3.** SEM images of (a, b) side views and (c) top view of sample synthesized at pH 9.0. (d) Schematic illustration of the 18-faceted polyhedral structure. (e) Homogeneous spindle-like sample prepared at pH 7.0. (f) A higher magnification SEM image shows the coarse surface of the spindles indicating the existence of defects.

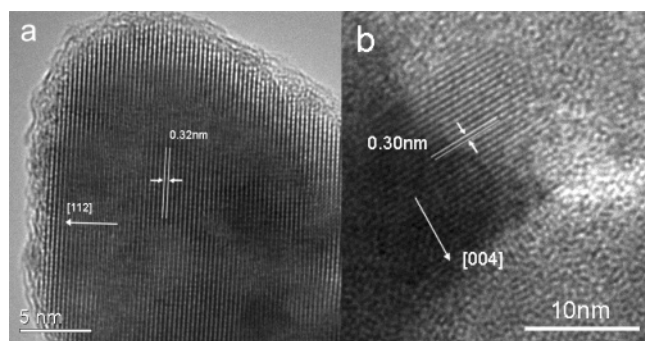


**Figure 4.** HRTEM images recorded on (a) the tip of a spindle, and (b) a single particle.

under ultrasound treatment the complex dissociated and in situ generated Pb<sup>2+</sup>. The coordinating strength of the initial Pb–NTA complexes formed under different conditions would affect the release speed and the monomer concentration of free Pb<sup>2+</sup> in the solution. WO<sub>4</sub><sup>2−</sup> in the solution then combined with the released Pb<sup>2+</sup> to yield PbWO<sub>4</sub> nuclei. These freshly formed nuclei are unstable and have the tendency to grow into larger grains due to their high chemical potential.<sup>22</sup>

**Effect of pH Value.** The pH value of reaction system is one of the most important factors. A pH range of 5–9 is optimal. If the pH value is higher than 11, another complex, Pb(OH)<sub>x</sub><sup>2−x</sup>, was formed due to the high concentration of OH<sup>−</sup> and the strong complexing ability between Pb<sup>2+</sup> and OH<sup>−</sup>. In this case, no product of PbWO<sub>4</sub> could be obtained. When the pH value was adjusted to 9, 7, and 5, products with different morphologies were achieved. With the decrease of pH value, the dimensions of the products decreased and the morphologies changed from 3D nanopolyhedrons to 1D spindle-like nanorods and then to 0D nanoparticles. The influence of pH on the morphologies may be explained as follows. Under pH 9–7, nitrilotriacetic acid exists as NTA<sup>3−</sup> and the predominant species in solution remains a 1:1 complex of PbNTA<sup>−</sup>. With pH decreasing, NTA<sup>3−</sup>

would partly combine H<sup>+</sup> in the solution. When pH was lower than 5, NTA<sup>3−</sup> would exist as H<sub>x</sub>NTA<sup>x−3</sup> and its complexing ability with metal ions would therefore decrease. According to Peng et al.,<sup>23</sup> a higher monomer concentration favors 1D-growth and lower monomer concentration favors 3D-growth. In our experiments, the pH 9.0 reaction system with the strongest coordination of Pb–NTA led to a relatively slow release of Pb<sup>2+</sup> and lower monomer concentration, which resulted in the formation of 3D structure. The pH 7.0 reaction system could provide a higher monomer concentration of free Pb<sup>2+</sup> due to the relatively weaker metal complexing association and faster release of Pb<sup>2+</sup>, which induced 1D-growth. In the case of the pH 5.0 system, nucleation occurred at an outburst speed right after the reaction solutions were mixed, leading to a large quantity of PbWO<sub>4</sub> precipitation and extremely low monomer concentration in the solution, so a small dot-shaped product was obtained under this situation.<sup>24</sup> This morphology evolution in our samples is similar to the result observed by Peng et al. in the synthesis of CdSe.<sup>24</sup>

**Effect of NTA Concentration.** The amount of the complexing agent also has an influence on the products. Figure 5 shows the TEM images of PbWO<sub>4</sub> nanocrystals prepared in the presence of different amounts of NTA at pH 9.0. We found that with the increase of the NTA/Pb ratio the as-prepared PbWO<sub>4</sub> nanocrystals became larger and it took more time for products to precipitate. With the concentration of NTA changed to 80 mM and all of the other preparation conditions remaining unchanged, the sample size increased to 1 μm<sup>2</sup>, as observed in Figure 5b. When the concentration of NTA increased to 160 mM, the size of the product became even larger, and its morphology changed to irregular (Figure 5a). With the ratio of NTA/Pb increasing, the initiative concentration of free Pb<sup>2+</sup> in the solution decreases. As a result, the nucleation rate of PbWO<sub>4</sub> becomes slower, which is favorable for the nuclei to grow into larger 3D grains. While the NTA/Pb ratio was chosen as 1:1, the





**Figure 5.** TEM images of products synthesized at pH 9.0 with NTA concentrations of (a) 160, (b) 80, and (c) 20 mM.

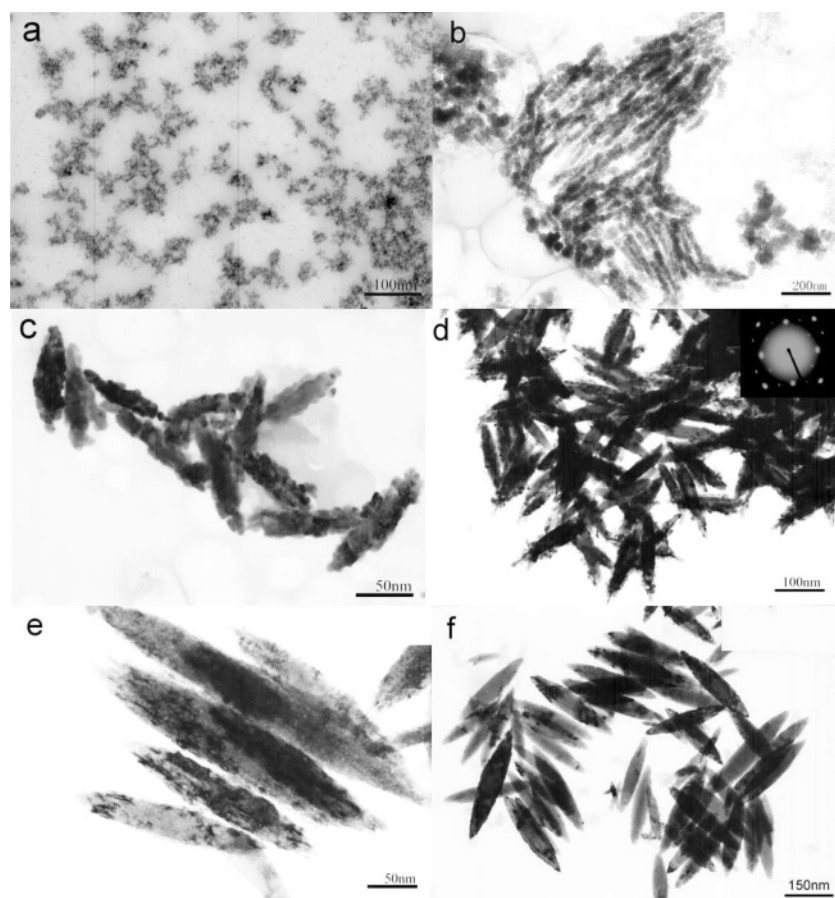


**Figure 6.** Time-dependent TEM images of spindle-like crystal after ultrasound treatment of (a) 40, (b) 50, (c) 60, (d) 70, (e) 90, and (f) 110 min. The nanoparticles aggregated on the backbones of the spindles leading to the coarse texture of the surfaces and indicating the aggregation-growth mechanism.

sample changed to spindle-like nanorods (Figure 5c) that are similar to the products prepared at pH 7 and with NTA/Pb ratio of 2:1. In this case, we assumed that the monomer concentration and nucleation rate under the two reactive conditions might be similar.

**Possible Growth Mechanism and Effect of Ultrasound Irradiation.** The growth process of the spindle-like structure was carefully followed by time-dependent experiments. TEM images obtained after different reaction times show an obvious growth process from small primary nanoparticles to the final spindles (Figure 6). With ultrasound treatment of 40 min, the transparent reaction solution became turbid, indicating the formation of nuclei, and 10 min later a white precipitate began to arise. Small primary particles were observed first (Figure 6a), and these nanoparticles further aggregated in some specific orientations (Figure

6b) to form spindle-like structures (Figure 6c). The texture of the spindles at this stage (sonication for 60 min) is quite loose (Figure 6c), and careful observation shows the spindles are composed of oriented-aggregated primary particles. Figure 6c–e clearly shows that the small particles spontaneously attached on the backbone of the spindles. Furthermore, the spindles with rather rough surfaces made of small primary building blocks were still perfect single crystals as confirmed by the electron diffraction patterns (inset of Figure 6d).

HRTEM images of a series of aggregated particles at the early stage of the crystal growth (Figure 7) give more details. The vast majority of particles appear to be composed of many primary building block particles ranging in size from less than 5 to 10 nm. It is seen that the lattice planes of the depicted particles are almost perfectly aligned. Moreover, the lattice planes

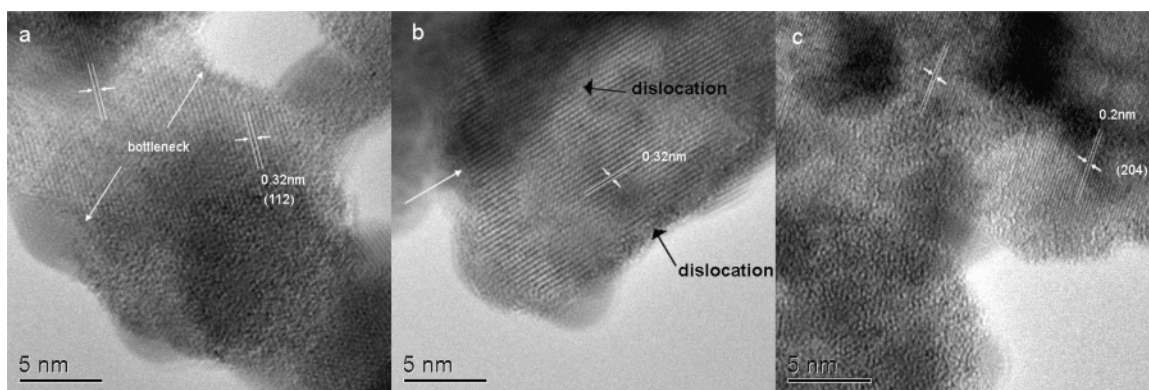


**Figure 7.** Typical HRTEM images of aggregated particles at the early stage of crystal growth. (a) Several nanoparticles fused after oriented attachment. The lattice planes of the connected particles are almost perfectly aligned. Bottlenecks between the adjacent particles are still visible. (b) Clear crystal lattice after oriented attachment. Black arrows highlight boundaries in which a slight misorientation between primary particles has been incorporated, and white arrows indicate boundaries in which there is no misorientation between primary particles. (c) Some oriented attachment occurs on  $\{204\}$ .

go straight through the contact areas; that is, the particles are epitaxially fused together; bottlenecks between the adjacent particles are still visible (Figure 7a). The perfect parallel fringes observed by HRTEM (Figure 7b) shows that all small nanoparticles are attached on the spindles with the same orientation. Also, edge dislocations at the interface between the two primary building block particles could be detected clearly (Figure 7b). In the majority of images, we find that oriented attachment occurs most commonly on  $\{112\}$  and occasionally on  $\{204\}$  (Figure 7c). These microstructural features yield important clues to mechanisms by which primary building blocks assemble to produce larger particles.

Such spontaneous “landing” of the small nanoparticles on the backbone of the spindles and then undergoing self-aggregation could be related to one proposed mechanism, so-called “orientated attachment” by Penn and Banfield et al.<sup>25,26</sup> In this mechanism, the bigger particles are grown from small primary nanoparticles through an orientated attachment process, in which the adjacent nanoparticles are self-assembled by sharing a common crystallographic orientation and docking of these particles at a planar interface.<sup>25</sup> Primary particles may aggregate in an oriented fashion to produce a larger single crystal, or they may aggregate randomly and reorient, recrystallize, or undergo phase transformations to produce larger single crystals. This kind of growth mode could lead to the formation of faceted particles or anisotropic growth if there is sufficient difference in the surface energies of different crystallographic faces.<sup>27</sup> In the so formed aggregates, the crystalline lattice planes may be almost perfectly aligned, or dislocations at the contact areas between the adjacent particles lead to defects in the finally formed bulk crystals.<sup>25</sup>

High-intensity ultrasound irradiation also played an important role in the formation of products. The transient high-temperature and high-pressure field produced during ultrasound irradiation provides a favorable environment for the anisotropic growth of nanocrystals. Cavitations and shock waves created by ultrasound can accelerate solid particles to high velocities leading to interparticle collisions and inducing effective fusion at the point of collision.<sup>28</sup> We consider it is ultrasound that caused the fusion of adjacent particles

and attachment of primary particles on the outlayers of the spindles. The energy generated during collision can induce the crystallization of the amorphous particles, responsible for the further crystallization process. Therefore, we believe that the sonochemical formation of spindle-like  $\text{PbWO}_4$  underwent three steps in sequence: (1) ultrasound-induced dissociation of  $\text{Pb-NTA}$  complex and formation of nuclei, which led to primary nanoparticles; (2) ultrasound-induced fusion of these primary nanoparticles accompanying oriented attachment to form the spindle-like structure; and (3) a further growth and crystallization process, giving rise to the formation of single crystalline product.

Yu et al. have synthesized  $\text{PbWO}_4$  with a micro-spindle structure through a hydrothermal route, and they also observed the growth process.<sup>13</sup> A similar oriented attachment growth mechanism was put forward. However, it is interesting that some nanopolyhedrons instead of nanoparticles were found to appear at the initial stage and further evolve into final spindles. The different intermediate materials apparently came from the different reaction systems. Nanoparticles in our experiment and the self-organization of these particles could be attributed to the special effects of high-intensity ultrasound irradiation.

**Raman Spectra.** The optical properties of these products were also studied. The Raman spectrum of the stolzite polyhedral structure (Figure 8) shows six bands in the range of  $100\text{--}1000\text{ cm}^{-1}$ . The peaks located at  $903.0$ ,  $764.8$ ,  $748.7$ ,  $353.3$ , and  $325.3\text{ cm}^{-1}$  correspond to the vibration modes  $\nu_1(\text{A}_g)$ ,  $\nu_3(\text{B}_g)$ ,  $\nu_3(\text{E}_g)$ ,  $\nu_2(\text{B}_g)$ , and  $\nu_2(\text{A}_g)$ , respectively, which are consistent with those reported previously.<sup>13,29</sup> The peak at  $175.2\text{ cm}^{-1}$  was not assigned by Ross,<sup>30</sup> but Griffith et al. observed a similar peak in natural and synthetic stolzite samples,<sup>31</sup> and this peak could be assigned as the translational mode of the  $\text{WO}_4$  group analogous to that for  $\text{CdMoO}_4$ .<sup>29</sup> The Raman spectra of crystals with other shapes (Figure S1 in Supporting Information) are similar to that of the polyhedral structures.

**Photoluminescence Properties.** Figure 9 shows the room-temperature photoluminescence spectra of the different nanostructures using the same excitation line at  $300\text{ nm}$ . The spectra show that all of the three samples exhibited typical green emission peaks at  $480\text{--}$

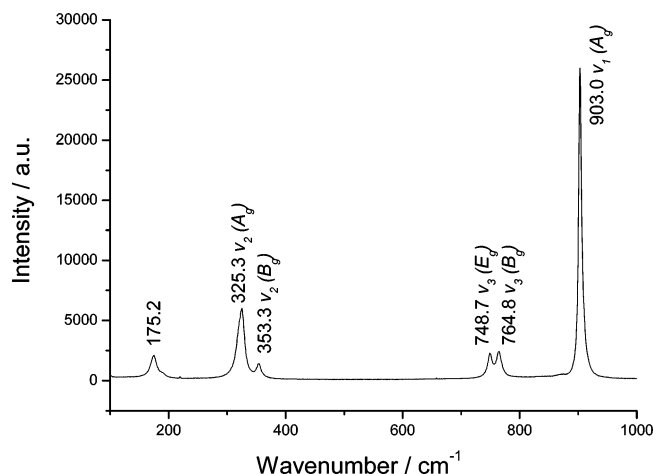


**Figure 8.** Raman spectrum of PbWO<sub>4</sub> polyhedral crystals.

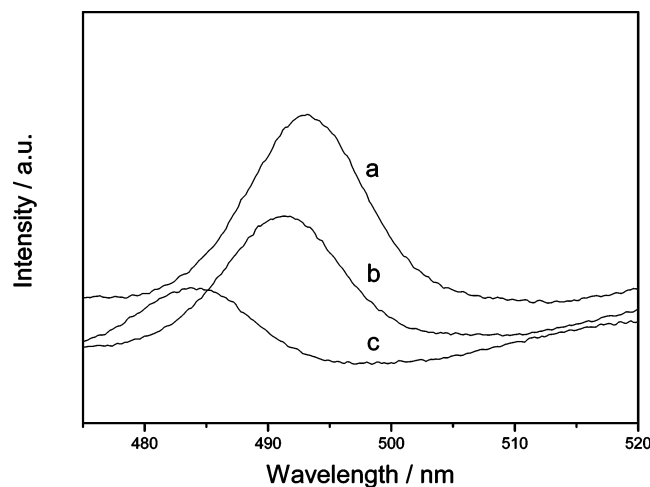


**Figure 9.** Room-temperature PL spectra of (a) polyhedral, (b) spindle-like, and (c) dot-shaped PbWO<sub>4</sub> samples.

500 nm, similar to the result reported by Shi et al.<sup>32</sup> The corresponding strongest emission peaks for polyhedral, spindle-like, and dot-shaped PbWO<sub>4</sub> nanostructures appear at 493, 491, and 483 nm, respectively. The peak value of dot-shaped sample is slightly smaller than the other two samples due to its small dimension. Very weak size-dependent phenomenon of PL properties observed between the polyhedral and spindle-like products indicates that the sizes of the two nanostructures are so big that they are beyond the border of the quantum confinement regime. Meanwhile, the relative intensities of the PL peaks seem closely related to the morphology and crystallinity. In the three samples, the polycrystalline product with dot-shaped morphology shows a weak luminescence, whereas the polyhedral sample with the best crystallinity displays the strongest luminescence under the same measurement conditions. The enhancement of PL intensity may be due to the improved crystallinity, which has similarly been observed by other researchers.<sup>33–35</sup> We also assume that polyhedral and spindle-like crystals would possess more defects so they show more intense PL emission, and the special 18-faceted polyhedral morphology may favor engendering high-intensity green luminescence. These results could indicate that luminescence properties of

PbWO<sub>4</sub> are very sensitive for its structure and strongly dependent on the crystallinity and structural defects.

## Conclusion

In summary, we have successfully synthesized tetragonal PbWO<sub>4</sub> nanocrystals with special structures via a simple and fast sonochemical route. Simply controlling the reaction conditions, such as the pH value and the amount of complexing reagent, polyhedral, spindle-like, and dot-shaped morphologies could be obtained. The formation mechanism of spindle-like structure has been investigated, and the ultrasound-induced oriented attachment process clearly contributes to the creation of such structure. Room-temperature photoluminescence of PbWO<sub>4</sub> samples with different morphologies has also been investigated, and the results reveal that all of these samples showed similar features with green emissions at 480–500 nm but different luminescence intensity. The optical properties of these PbWO<sub>4</sub> nanocrystals differ from those of the bulk crystals, which could be related to their structural specialty and defects.

**Acknowledgment.** This work is supported by the National Natural Science Foundation of China (Grant Nos. 20325516 and 90206037), and we also thank Professor Yi-Nong Lv for his skillful measurement on HRTEM.

**Supporting Information Available:** Raman spectra of spindle-like and dot-shaped PbWO<sub>4</sub> samples. This material is available free of charge via the Internet at <http://pubs.acs.org>.

## References

- (1) (a) Lieber, C. M. *Solid State Commun.* **1998**, *107*, 607. (b) Alivisatos, A. P. *Science* **1996**, *271*, 933.
- (2) Xia, Y.; Yang, P.; Sun, Y.; Wu, Y.; Mayer, B.; Gates, B.; Yin, Y.; Kim, F.; Yan, H. *Adv. Mater.* **2003**, *15*, 353.
- (3) Mdleleni, M. M.; Hyeon, T.; Suslick, K. S. *J. Am. Chem. Soc.* **1998**, *120*, 6189.
- (4) Gedanken, A. *Ultrason. Sonochem.* **2004**, *11*, 47.
- (5) Okitsu, K.; Yue, A.; Tanabe, S.; Matsumoto, H.; Yobiko, Y.; Yoo, Y. B. *Chem. Soc. Jpn.* **2002**, *75*, 2289.
- (6) Suslick, K. S.; Choe, S. B.; Cichowlas, A. A.; Grinstaff, M. W. *Nature* **1991**, *353*, 414.
- (7) Kobayashi, M.; Ishii, M.; Usuki, Y. *Nucl. Instrum. Methods Phys. Res., Sect. A* **1998**, *406*, 442.
- (8) Hara, K.; Ishii, M.; Kobayashi, M.; Nikl, M.; Takano, H.; Tanaka, M.; Tanji, K.; Usuki, Y. *Nucl. Instrum. Methods Phys. Res., Sect. A* **1998**, *414*, 325.
- (9) Nitsch, K.; Nikl, M.; Ganschow, S.; Reiche, P.; Uecker, R. *J. Cryst. Growth* **1996**, *165*, 163.
- (10) Tanji, K.; Ishii, M.; Usuki, Y.; Kobayashi, M.; Hara, K.; Takano, H. *J. Cryst. Growth* **1999**, *204*, 505.
- (11) An, C. H.; Tang, K. B.; Shen, G. Z.; Wang, C. R.; Qian, Y. T. *Mater. Lett.* **2002**, *57*, 565.
- (12) Hu, X. L.; Zhu, Y. *J. Langmuir* **2004**, *20*, 1521.
- (13) Liu, B.; Yu, S. H.; Li, L. J.; Zhang, Q.; Zhang, F.; Jiang, K. *Angew. Chem., Int. Ed.* **2004**, *43*, 4745.
- (14) Chen, D.; Shen, G. Z.; Tang, K. B.; Liang, Z.; Zheng, H. G. *J. Phys. Chem. B* **2004**, *108*, 11280.
- (15) Klug, H.; Alexander, L. *X-ray Diffraction Procedures*; Wiley: New York, 1962; p 125.
- (16) Pan, L.; Ching, N.; Huang, X. *Chem.-Eur. J.* **2001**, *7*, 4431.
- (17) Banaszak, J. E.; Rittmann, B. E.; Reed, D. T. *J. Radioanal. Nucl. Chem.* **1999**, *241*, 385.
- (18) Martin, L. L.; Jacobson, R. A. *Inorg. Chem.* **1972**, *11*, 2785.
- (19) Chen, Y.; Ma, B. Q.; Liu, Q. D.; Li, J. R.; Gao, S. *Inorg. Chem. Commun.* **2000**, *3*, 377.
- (20) Suslick, K. S. *Ultrasound: Its Chemical, Physical and Biological Effects*; VCH: Weinheim, Germany, 1988.

- (21) Suslick, K. S.; Hammerton, D. A.; Cline, R. E. *J. Am. Chem. Soc.* **1986**, *108*, 5641.
- (22) Sugimoto, T. *Adv. Colloid Interface Sci.* **1987**, *28*, 65.
- (23) Peng, Z. A.; Peng, X. G. *J. Am. Chem. Soc.* **2001**, *123*, 1389.
- (24) Peng, X. G. *Adv. Mater.* **2003**, *15*, 459.
- (25) Penn, R. L.; Banfield, J. F. *Science* **1998**, *281*, 969.
- (26) Banfield, J. F.; Welch, S. A.; Zhang, H. Z.; Ebert, T. T.; Penn, R. L. *Science* **2000**, *289*, 751.
- (27) Penn, R. L.; Oskam, G.; Strathmann, T. J.; Searson, P. C.; Stone, A. T.; Veblen, D. R. *J. Phys. Chem. B* **2001**, *105*, 2177.
- (28) Doktycz, S. J.; Suslick, K. S. *Science* **1990**, *247*, 1067.
- (29) Crane, M.; Frost, R. L.; Williams, P. A.; Klopogge, J. T. *J. Raman Spectrosc.* **2002**, *33*, 62.
- (30) Ross, S. D. *Inorganic Infrared and Raman Spectra*; McGraw-Hill: Maidenhead, 1972.
- (31) Bastians, S.; Crump, G.; Griffith, W. P.; Withnall, R. *J. Raman Spectrosc.* **2004**, *35*, 726.
- (32) Shi, C. S.; Wei, Y. G.; Yang, X. Y.; Zhou, D. F.; Guo, C. X.; Liao, J. Y.; Tang, H. G. *Chem. Phys. Lett.* **2000**, *328*, 1.
- (33) Yu, M.; Lin, J.; Fang, J. *Chem. Mater.* **2005**, *17*, 1783.
- (34) Bae, J. S.; Kim, S. B.; Jeong, J. H.; Park, J. C.; Kim, D. K.; Byeon, S. H.; Yi, S. S. *Thin Solid Films* **2005**, *471*, 224.
- (35) Soledade, L. E. B.; Longo, E.; Leite, E. R.; Pontes, F. M.; Lanciotti, F.; Campos, C. E. M.; Pizani, P. S.; Varela, J. A. *Appl. Phys. A* **2002**, *75*, 629.

CG050235S